Surface charge of polyoxometalates modulates polymerization of the scrapie prion protein

Holger Wille[a,b,1], Maheswaran Shanmugam[a,c], Muralee Murugesu[a,c,2], Julian Ollesch[a], Gerald Stubbs[d], Jeffrey R. Long[a,c], Jiri G. Safar[a,b,3], and Stanley B. Prusiner[a,b,1]

[a]Institute for Neurodegenerative Diseases and [b]Department of Neurology, University of California, San Francisco, CA 94143; [c]Department of Chemistry, University of California, Berkeley, CA 94720; and [d]Department of Biological Sciences and Center for Structural Biology, Vanderbilt University, Nashville, TN 37235

Contributed by Stanley B. Prusiner, December 31, 2008 (sent for review October 13, 2008)

Prions are composed solely of an alternatively folded isoform of the prion protein (PrP), designated PrP^{Sc}. N-terminally truncated PrP^{Sc}, denoted PrP 27–30, retains infectivity and polymerizes into rods with the ultrastructural and tinctorial properties of amyloid. We report here that some polyoxometalates (POMs) favor polymerization of PrP 27-30 into prion rods, whereas other POMs promote assembly of the protein into 2D crystals. Antibodies reacting with epitopes in denatured PrP 27-30 also bound to 2D crystals treated with 3 M urea. These same antibodies did not bind to either native PrP^{Sc} or untreated 2D crystals. By using small, spherical POMs with Keggin-type structures, the central heteroatom was found to determine whether prion rods or 2D crystals were preferentially formed. An example of a Keggin-type POM with a phosphorous heteroatom is the phosphotungstate anion (PTA). Both PTA and a Keggin-type POM with a silicon heteratom have low-charge densities and favor formation of prion rods. In contrast, POMs with boron or hydrogen heteroatoms exhibiting higher negative charges encouraged 2D crystal formation. The 2D crystals of PrP 27-30 produced by selective precipitation with POMs were larger and more well ordered than those obtained by sucrose gradient centrifugation. Our findings argue that the negative charge of Keggin-type POMs determines the quaternary structure adopted by PrP 27-30. The mechanism by which POMs function in competing prion polymerization pathways—one favoring 2D crystals and the other, amyloid fibrils—remains to be established.

2D crystal | amyloid | electron crystallography | ImmunoGold labeling | phosphotungstate

Prion diseases such as scrapie, Creutzfeldt–Jakob disease, and bovine spongiform encephalopathy are caused by an alternatively folded prion protein (PrP) isoform, designated PrP^{Sc} (1, 2). A profound conformational change features in the conversion of the cellular precursor PrP^{C} into PrP^{Sc} (3, 4). PrP^{Sc} is highly lipophilic and resistant to solubilization in nondenaturing detergents, whereas PrP^{C} is readily solubilized by such detergents (5–7). The insolubility of PrP^{Sc} has prohibited high-resolution structural studies by X-ray crystallography or NMR spectroscopy (8, 9).

Early observations on the quaternary structure of prions came from sucrose gradient fractions highly enriched for prion infectivity (10). These fractions contained N-terminally truncated PrP^{Sc}, denoted PrP 27-30, and numerous rod-shaped particles with the ultrastructural and tinctorial properties of amyloid (5). The prion rods retained all of the infectivity exhibited by amorphous aggregates of full-length PrP^{Sc}. In addition to the prion rods, the sucrose gradient fractions also contained 2D crystals that appear to be alternative quaternary structures of PrP 27-30 (11, 12). Optical spectroscopy indicated high β-sheet structure for both PrP 27-30 and full-length PrP^{Sc} (3, 4). Additionally, antibody mapping studies argue that refolding of PrP^{C} into PrP^{Sc} occurs in a region between residues 90 and 176 (13, 14).

For many years, the detection of PrP^{Sc} was based on the immunodetection of PrP 27-30 that was generated after limited proteolysis catalyzed by proteinase K, which digested the precursor PrP^{C} (15, 16). During the development of an improved immunoassay, we found that salts of the phosphotungstate anions (PTA; $Na_2H[PW_{12}O_{40}]$) selectively precipitate PrP^{Sc} (17).

We report here that PTA precipitation can be used in place of sucrose gradient centrifugation for the preparation of 2D crystals of PrP 27-30 and that a series of compounds with structures similar to PTA (18) controls the quaternary structure of PrP 27-30. By using small, spherical POMs with Keggin-type structures (19), the central heteroatom was found to determine whether prion rods or 2D crystals were preferentially formed. Both PTA and a Keggin-type POM with a silicon heteratom have low charge densities and favor formation of prion rods. In contrast, POMs with boron or hydrogen heteroatoms exhibiting higher negative charges encouraged 2D crystal formation. The 2D crystals of PrP 27-30 produced by selective precipitation by using POMs were larger and more well ordered than those obtained by protocols employing sucrose gradient centrifugation. Our findings argue that the negative charge of Keggin-type POMs determines the quaternary structure adopted by PrP 27-30. Large and highly organized crystals are essential for high-resolution analyses by cryo low-dose electron crystallography. Whether POMs can be used to create well-ordered 3D crystals amenable to atomic structure determinations is unknown.

Results

2D Crystals Composed of PrP 27-30. In fractions purified by sucrose gradient centrifugation, we initially found numerous rods composed of PrP 27-30 (5). Subsequently, we identified 2D crystals in these same fractions (Fig. 1*A*) (11, 12). Because these fractions contained primarily one protein by silver staining, we concluded that both the rods and 2D crystals were composed of PrP 27-30 (Fig. 1*D*). Using Keggin-type POMs, we found larger and more ordered 2D crystals (Fig. 1 *B* and *C*) than previously observed in the sucrose gradient preparations. As shown by silver staining and Western blot analysis, the crystals appear to be composed of PrP 27-30 (Fig. 1*E*). The silver-stained bands from the PTA precipitate are primarily N-terminally truncated glycoforms of PrP^{Sc} (Fig. 1*E*, lane 3). When the ammonium salt of the POM HTA $(NH_4)_6[H_2W_{12}O_{40}]$ was used to precipitate PrP 27-30, the

Author contributions: H.W., J.R.L., J.G.S., and S.B.P. designed research; H.W. performed research; M.S., M.M., J.O., and J.R.L. contributed new reagents/analytic tools; H.W., G.S., and J.G.S. analyzed data; and H.W., J.G.S., and S.B.P. wrote the paper.

The authors declare no conflict of interest.

[1]To whom correspondence may be addressed. E-mail: hwille@ind.ucsf.edu or stanley@ind.ucsf.edu.

[2]Present address: Department of Chemistry, University of Ottawa, Ottawa, ON, Canada K1N 6N5.

[3]Present address: National Prion Disease Pathology Surveillance Center, Department of Pathology, Case Western Reserve University, Cleveland, OH 44106.

This article contains supporting information online at www.pnas.org/cgi/content/full/0812770106/DCSupplemental.

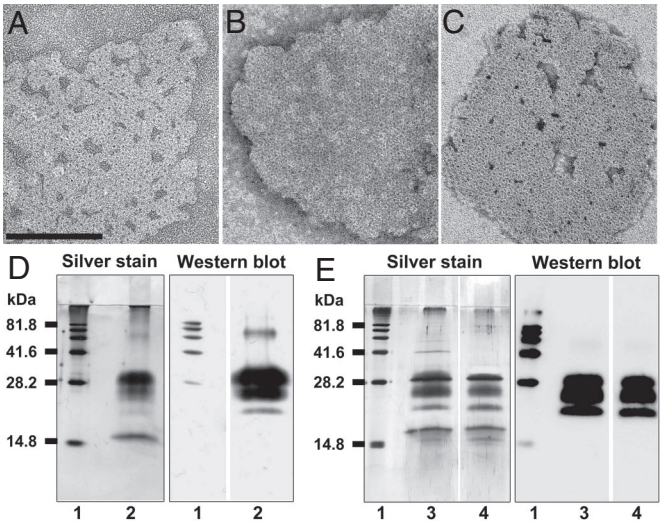

Fig. 1. Two-dimensional crystals of PrP 27-30 prepared by different purification protocols: traditional sucrose-gradient procedure (10) (*A*), precipitation with PTA (*B*), and precipitation with HTA (*C*). The 2D crystals from the sucrose-gradient procedure tended to be smaller and contained more defects than those obtained by POM precipitation. For all 3 preparations, the lattice parameters were essentially identical (a and b = 6.9 nm; γ = 120°) and as previously determined (11, 12). (Scale bar: *A*, 100 nm; applies to all micrographs.) (*D* and *E*) SDS/PAGE analysis of a sucrose gradient–derived sample (*D*) and of samples from POM precipitations (*E*). After SDS/PAGE, gels were silver-stained or immunoblotted by using anti-PrP polyclonal antiserum W5517, as labeled. Lanes 1, molecular mass standards, in kilodaltons (kDa), that can be visualized in silver stains and Western blots (Chemicon). PrP 27-30 samples purified by the sucrose-gradient protocol (lanes 2), precipitated with PTA (lanes 3) or with HTA (lanes 4). Although the bands of PrP 27-30 from sucrose gradient purification are the dominant protein bands, a small contaminating peptide of ≈16 kDa can also be seen (*D*). In comparison, samples precipitated by the POMs (*E*) consist mostly of PrP 27-30 with a few contaminating peptides at ≈16 kDa. PrP 27-30 samples purified by sucrose gradient (*A* and *D*) were derived from Syrian hamster Sc237 prions; samples purified by PTA and HTA (*B*, *C*, and *E*) were derived from mouse RML prions.

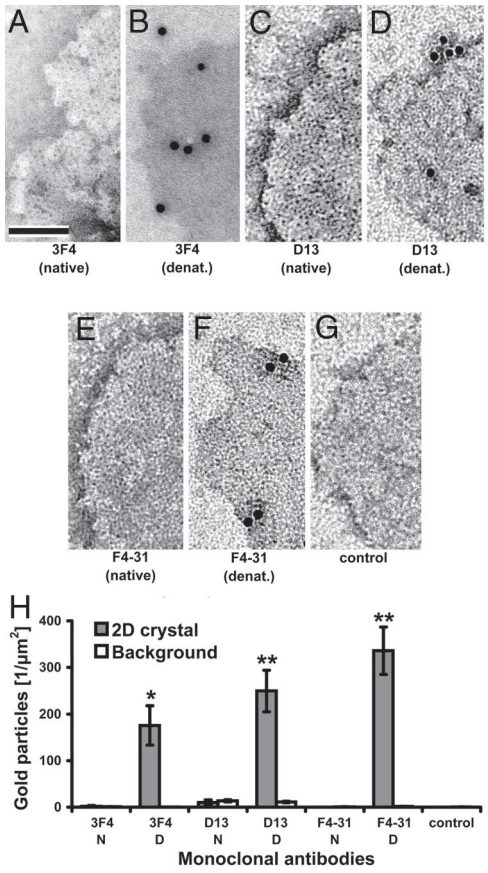

Fig. 2. ImmunoGold labeling of native (*A*, *C*, and *E*) and denatured (*B*, *D*, *F*, and *G*) 2D crystals. Denaturation with urea before immunolabeling made it more difficult to discern the crystalline lattice. Crystals were incubated with anti-PrP monoclonal antibodies F4-31 (*A* and *B*), D13 (*C* and *D*), 3F4 (*E* and *F*), and without primary antibody (*G*). (*H*) Bar graph showing a quantitative analysis of the immunolabeling densities for the 3 antibodies. F4-31, D13, and 3F4 showed significantly greater labeling with denatured compared with native 2D crystals (*, $P < 0.005$; **, $P < 0.001$; Table 1). The values for the background labeling are similar to those for native 2D crystals. In many instances, the bars and error bars of the control and background measurements were too small to be visible at this scale. (Scale bar: *A*, 50 nm; applies to *B*–*G*.)

silver-stained band at the top of the polyacrylamide gel diminished, suggesting improved purification (Fig. 1*E*, lane 4). The band at ≈16 kDa was found with all 3 purification protocols; extracts of this band from the gel produced no interpretable signal by mass spectrometry analysis. This observation suggests that the ≈16-kDa band may consist of several different polypeptides.

Still concerned that the crystals might be composed of a non-PrP^{Sc} minor contaminant, we undertook a quantitative immunostaining EM study. Previously, we found that the 3F4 mAbs bound to the 2D crystals after exposure to 2 M urea (12). Because quantification of the findings with 3F4 mAbs produced results of limited statistical significance, we selected 2 other mAbs, D13 and F4–31, that bind to epitopes that are exposed in denatured PrP^{Sc} but buried in native PrP^{Sc}. All 3 antibodies, D13, F4–31 and 3F4 failed to bind native 2D crystals (Fig. 2 *A*, *C*, and *E*) but recognized PrP^{Sc} after exposure to 3 M urea (Fig. 2 *B*, *D*, and *F*). By using 3 M urea, all 3 α-PrP mAbs showed statistically significant differences between binding to native and denatured crystals (Fig. 2*H* and Table 1). The *P* value for labeling density of native versus denatured 2D crystals with the 3F4 mAb was <0.005, and the *P* values for D13 Fab and F4–31 mAb were <0.001. These findings argue that the 2D lattices are formed of native conformers of PrP 27-30 with buried epitopes, which become exposed after treatment with 3 M urea.

POM-Mediated Crystallization of PrP 27-30. In an effort to improve the 2D crystallization procedure, we tested the effects of ionic and nonionic detergents, proteases, buffers, chelators, lipids, and other additives [supporting information (SI) Table S1]. More than 300 grids were stained and inspected for the presence of 2D crystals; ≈30% of the samples contained 2D crystals (Fig. S1*a*). Neither 2D crystals nor prion rods were found in fractions prepared from the brains of uninoculated mice (Fig. S1*c*).

Several of the additives increased the yield of 2D crystals (Table S1), but none improved their quality. For example, we observed that higher concentrations of proteinase K (PK) increased the yield, even though the N-terminal truncation of PrP^{Sc} to form PrP 27-30 was accomplished at lower concentrations of PK as judged by Western blot analysis. These findings raised the possibility that protein or peptide contaminants adversely affect 2D crystallization. Impurities may hinder 2D crystallization by binding to the crystal lattice, preventing the lattice from extending. A comparison of silver-stained gels and Western blots revealed that PrP 27-30 was only a minor component at this stage of the preparation. Considering the amount of impurities, it is surprising that PrP 27-30 crystallized at all. The importance of protein purity and homogeneity for 2D crystallization is well recognized (20, 21).

Because we had found that PTA, $[PW_{12}O_{40}]^{3-}$, selectively

Table 1. Quantification of the ImmunoGold labeling

	Native					Denatured*					
	2D crystal		Background			2D crystal		Background			
Antibody	*N*	*N*/μm^2	*N*	*N*/μm^2	*P*†	*N*	*N*/μm^2	*N*	*N*/μm^2	*P*†	*P*‡
F4-31	0	0.00	20	0.64	0.032	135	335.81	44	1.41	<0.001	<0.001
D13	5	9.96	418	13.41	0.576	111	249.39	341	11.06	<0.001	<0.001
3F4	1	1.77	16	0.91	0.646	42	175.58	5	0.23	<0.002	<0.005
Control§	0	0.00	1	0.09	0.423	0	0.00	11	0.42	0.093	n.d.

*Grids treated with 3 M urea prior to the ImmunoGold labeling.
†*P* value for labeling density of 2D crystal versus background.
‡*P* value for labeling density of native versus denatured 2D crystal.
§No primary antibody used. n.d., not determined.

precipitates PrP^{Sc} and PrP 27-30 (17), we asked whether PTA might be used to isolate 2D crystals. Using PTA, we found both prion rods and 2D crystals (Fig. S1 *d* and *e*). The crystals were generally of higher quality than the best 2D crystals obtained by any of the other protocols previously used. Preparations from the brains of uninoculated control animals consistently failed to show any 2D crystals or prion rods (Fig. S1*f*), supporting the argument that the 2D crystals are composed of PrP 27-30. Image processing revealed the amount of structural detail that can be resolved from these 2D crystals (Fig. S2).

Within the framework of the PTA precipitation method, relatively minor changes in the purification procedure had major effects on 2D crystallization. For example, when we added the detergent Sarkosyl after the initial centrifugation used for clarification (see *Methods*), the amount of contaminating lipids was reduced, which, in turn, led to a noticeable increase in the yield of 2D crystals. Doubling the concentration of the brain homogenate from 5% to 10% (wt/vol) in the PTA precipitation step also increased the yield of 2D crystals. In both cases, the protein:lipid and the protein:detergent ratios were modified. The relative proportions of protein, lipid, and detergent are well-known factors influencing the 2D crystallization of membrane proteins (20, 21).

Despite its ability to increase the yield of 2D crystals, PTA failed to stain previously formed 2D crystals. Other heavy metal stains, such as uranyl acetate or ammonium molybdate, were successfully used to visualize 2D crystals of PrP 27-30 (11, 12). In contrast, prion rods were decorated with PTA (17). Apparently, the PTA binding site is not available in the 2D crystals and may participate in forming crystallographic contacts. The removal of PTA via dialysis further improved the yield and quality of the 2D crystals, reduced the number of prion rods. Presumably, dialysis caused the partial disassembly of the PTA/prion rod complexes, thereby increasing the amount of nonfibrillar, crystallization-competent PrP 27-30. Alternatively, PTA-bound PrP 27-30 may not be able to form 2D crystals on account of interference by PTA.

Precipitation of PrP 27-30 by Using Other Polyoxometalates. Given the improvements in 2D crystallization that were observed by employing PTA, we decided to explore other parameters related to the nature of the POM and their effect on PrP 27-30 (Table 2). We tested AsTA ($Na_{28}[As_4W_{40}O_{140}]$), TTA ($Na_{16}[Zn_4(H_2O)_2(P_2W_{15}O_{56})_2]$), and 4 Keggin-type POMs (Fig. 3*A*) for their ability to precipitate PrP 27-30 and analyzed the resulting pellets by quantitative electron microscopy and a conformation-dependent immunoassay (CDI) (Fig. 3*B*). In addition to PTA, the Keggin-type POMs evaluated were SiTA ($Na_4[SiW_{12}O_{40}]$), BTA ($K_5[BW_{12}O_{40}]$), and HTA ($(NH_4)_6[H_2W_{12}O_{40}]$). The yield of fibrils was quantified by taking advantage of the inherent electron density and the contrast of the POM·PrP 27-30 complexes (17). Fibrils were seen in all samples, but the quantities varied depending on which species of POM was used. Initially, we expected that, for the different POMs, the fibril content would correlate directly with the yield of precipitated PrP 27-30 as determined by CDI (17). However, the correlation between the fibril and PrP 27-30 contents was poor, with a coefficient of determination (r^2) of 0.20 (Fig. 3*B*).

On closer examination, two of the POMs (BTA and HTA) produced substantial numbers of aggregates other than fibrils, e.g., 2D crystals. The other POMs produced predominantly fibrillar aggregates and relatively few other structures. The propensity to form nonfibrillar structures explained the poor correlation between the fibril and the PrP 27-30 contents (Fig. 3*B*). When the data for BTA and HTA were excluded, the correlation between the fibril and PrP 27-30 contents was excellent, with an r^2 of 0.91 (Fig. 3*B*, solid line).

Impact of POM Charge on 2D Crystallization. We next examined whether the charge of the POM might modify polymeric forms of PrP 27-30. Keggin-type POMs have diameters of ≈1 nm and

Table 2. Properties of the different POMs

POM	POM anion	Negative charges*	Diameter, nm†	Molecular mass‡	POM structure§
PTA	$[PW_{12}O_{40}]^{3-}$	3	1.0	2,946	Keggin type
SiTA	$[SiW_{12}O_{40}]^{4-}$	4	1.0	2,966	Keggin type
BTA	$[BW_{12}O_{40}]^{5-}$	5	1.0	2,972	Keggin type
HTA	$[H_2W_{12}O_{40}]^{6-}$	6	1.0	2,986	Keggin type
AsTA	$[As_4W_{40}O_{140}]^{28-}$	28	2.5¶	10,537	Wheel-like
TTA	$[Zn_4(H_2O)_2(P_2W_{15}O_{56})_2]^{16-}$	16	2.5¶	8,097	Double Wells–Dawson type

*Of the intact POM at acidic pH.
†Measured along the longest axis of the molecule.
‡Calculated as a neutral sodium salt.
§See Fig. 3 and ref. 18.
¶Nonspherical molecule.

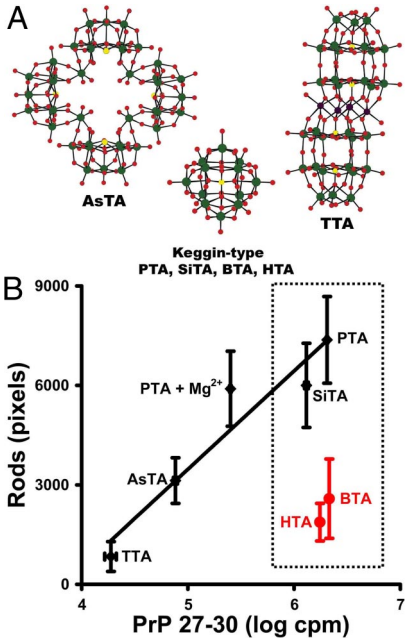

Fig. 3. Quantitative electron microscopy on fibrillar complexes of PrP 27–30 with 6 different POMs. (*A*) Stick-and-ball models of 3 different POM structures used. For all structures, oxygen is shown as red spheres and tungsten as green spheres. The yellow spheres represent arsenic in AsTA, phosphorus in TTA, and the central heteroatom (P, Si, B, H) in the Keggin-type POMs. In TTA, purple spheres represent zinc. (*B*) Correlation between the amount of PrP 27-30 as measured by CDI (abscissa) and the amount of fibrillar aggregates as determined by quantitative electron microscopy (ordinate). Overall, the correlation between the 2 measurements is rather poor, with a coefficient of determination (r^2) of 0.20. Excluding the values for BTA and HTA (see text) improves the correlation substantially ($r^2 = 0.91$; solid line). The error bars for the fiber quantification represent SEMs. The error bars for the CDI values represent the standard deviation; most CDI error bars are smaller than the symbols in the graph. The box delineates the data for the Keggin-type POMs.

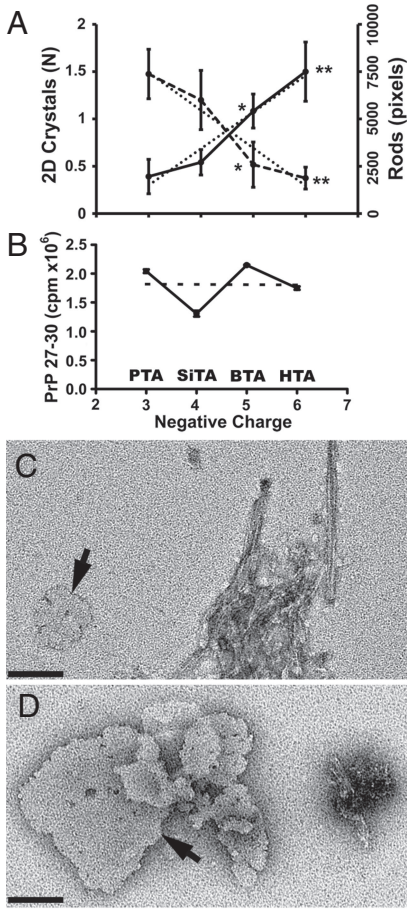

Fig. 4. Inverse correlation between the amounts of prion rods and 2D crystals in preparations with different Keggin-type POMs. (*A*) With increasing charge density of Keggin-type POMs, the amount of prion rods decreased (dashed-line curve) as the amount of 2D crystals increased (solid curve), as determined by quantitative electron microscopy. The reductions in fibril content from PTA to BTA (factor, ≈2.9) and to HTA (factor, ≈3.9) were statistically significant, with $P = 0.015$ (*) and $P = 0.002$ (**), respectively. The correlation coefficient (r) for all 4 POMs is −0.97 (dotted line). The increases in 2D crystal content from PTA to BTA (factor, ≈4.0) and to HTA (factor, ≈4.3) were statistically significant, with $P = 0.009$ (*) and $P = 0.001$ (**), respectively. For all 4 POMs, $r = 0.93$. Because different methods of quantification were used for the prion rods and 2D crystals, different scales are shown. The error bars represent SEMs. (*B*) The negative charge of the Keggin-type POMs and the amount of precipitated PrP 27-30, as determined by CDI, are not correlated ($r = -0.01$, dashed line). The error bars show the standard deviation. (*C* and *D*) Electron micrographs of negatively stained PrP 27-30 precipitated with PTA (*C*) and HTA (*D*). Arrows indicate 2D crystals with prion rods to the right; note the different amounts of 2D crystals and prion rods resulting from the 2 POMs. (Scale bar: 100 nm.)

share the same basic structure (19, 22, 23), but differ in their composition with respect to the central heteroatom (Fig. 3*A*). With the series of different heteroatoms (P, Si, B, and H), the charge density of the intact Keggin-type POMs increases linearly with the decreasing valency of the central heteroatom (Table 2).

A substantial decrease in the number of amyloid fibrils was observed from the series PTA < SiTA < BTA < HTA (Fig. 4), which correlated with the increasing negative charge of the POM species. In contrast, the amount of total PrP 27-30 detected by CDI showed no correlation with the charge of the POM (Fig. 4*B*). From these data, we conclude that higher-charged Keggin-structured POMs show a reduced propensity to induce formation of prion rods.

To determine whether the POM charge affected 2D crystallization, we quantified the total area covered by the 2D crystals and the number of crystals for the series of Keggin-type POMs (Fig. 4 *C* and *D*). A positive correlation was observed between the total area of 2D crystals as well as the number of crystals and the charge density of the intact Keggin-type POMs. HTA dramatically improved both the number and quality of the 2D crystals (Fig. 4 *A* and *D*).

Our observation that the 2D crystal and prion rod content vary inversely as a function of the charge density of the Keggin-type POM is puzzling. An earlier investigation of the solution properties of these POMs suggested that, under conditions similar to those used here, PTA, SiTA, and BTA dissociate into lacunary complexes by loss of a single $[WO]^{4+}$ unit (18, 24). This dissociation should increase the negative charge of the resulting lacunary structures to $[PW_{11}O_{39}]^{7-}$, $[SiW_{11}O_{39}]^{8-}$, $[HBW_{11}O_{39}]^{8-}$, respectively (compare the supporting information of ref. 18), thereby abolishing any meaningful correlation between the charge density and quaternary structure of PrP 27-30. It is conceivable, however, that the solution structure of the POMs does not represent the form that actually binds to prions. Additional investigations are needed to clarify what POM species is responsible for binding to PrP 27-30 and how the quaternary structure is affected by it.

Discussion

In the studies reported here, we present 5 different lines of evidence that the 2D crystals found in our preparations are composed largely of PrP 27-30. First, the 2D crystals were only found in fractions prepared from the brains of mice and hamsters infected with prions. No crystalline structures were found in

control fractions prepared from the brains of uninfected rodents. Second, two different purification protocols used for enriching PrP 27-30 and prion infectivity produced fractions containing both prion rods and 2D crystals (Fig. 1). One protocol used sucrose gradient centrifugation and the other used POM precipitation. Third, purified fractions containing rods and crystals had predominantly one protein, PrP 27-30, as demonstrated by silver staining; the protein was identified by immunostaining on Western blots (Fig. 1). Fourth, the diameter of the 2D crystal unit cells (Fig. 1) is similar to the diameter of negatively stained prion rod protofilaments. Fifth, α-PrP mAbs immunostained the 2D crystals (Fig. 2) (12). Taken together, these 5 lines of evidence argue that the 2D crystals found in purified fractions enriched for prion infectivity are composed largely, if not entirely, of PrP 27-30.

Because the number of 2D crystals is relatively small compared with the plethora of rods even under conditions that favor 2D crystal formation (Fig. 4), we were unable to apply techniques like optical spectroscopy to measure directly the β-sheet content of PrP 27-30 in the crystals. However, several lines of investigation argue that the PrP 27-30 molecules in the 2D crystals possess a conformation similar to that found in the rods (3–5). First, the epitopes in PrP 27-30 that are inaccessible to antibody binding when the protein is polymerized into prion rods are also buried in the 2D crystals (13, 14). These cryptic epitopes in both the rods and crystals were exposed by denaturants such as 3 M urea (Fig. 2 and Table 1) (12). Second, PrP 27-30 in prion rods and 2D crystals showed similar levels of resistance to digestion by proteinase K, in contrast to PrP^C, which is readily degraded by proteases. Third, PrP 27-30 in both the 2D crystals and the rods binds to POMs (Fig. 4), whereas PrP^C does not form precipitable complexes with POMs (17, 18, 25). Our results argue that the prion rods and 2D crystals represent alternative quaternary structures of PrP 27-30, but it seems likely that variations in the tertiary structure of PrP 27-30 are responsible for these two distinct polymeric forms.

The binding of a panel of mAbs directed to an array of epitopes in PrP 27-30 provides a sensitive tool for comparing the structure of PrP 27-30 in rods and 2D crystals. The R1 and R2 Fabs directed at the C terminus of PrP 27-30 reacted with native rods and crystals (12). As reported here, the 3F4 and F4–31 mAbs as well as the D13 Fab did not react with PrP 27-30 in native rods and crystals but did bind to the protein after exposure to 3 M urea. The concurrent behavior of PrP 27-30 immunoreactivity in the rods and crystals contend that the conformation of the protein is likely to be similar in these two macromolecular complexes. Our findings with PrP 27-30 contrast with studies on fibrillar and crystalline forms of insulin. In crystals, native insulin has an α-helical structure, whereas it acquires substantial β-sheet as it undergoes aggregation to form fibrils (26, 27).

The mechanisms that initiate and propagate rod and crystal formation are unknown. The prion rods are amyloid and undoubtedly form more readily when seeds are available to initiate the elongation. This phenomenon has been well studied for PrP amyloids (5, 28–30) as well as for amyloids formed from many other proteins (31, 32). Whether such seeds also initiate the formation of 2D crystals is unknown.

In addition to showing that the 2D crystals were composed of PrP 27–30 (Figs. 1 and 2), we found an inverse relationship between the number of rods and 2D crystals in purified prion fractions. POMs with low negative surface charges, such as PTA, favored the formation of rods, whereas those with high negative surface charges, such as HTA, favored the assembly of 2D crystals (Fig. 4).

Our finding that Keggin-type POMs can alter the amyloidogenic properties of PrP 27-30 expands the repertoire of effects that can be attributed to the interaction of POMs with proteins. The relatively high-charge density characteristic of some POMs is likely to be responsible for their interaction with proteins such as human serum albumin (33). The protein-binding capacity of polystyrene nanoparticles is also governed by both their size and surface properties (34). Furthermore, the correlation of the polymerization state of PrP 27-30 with the charge density of the POM indicates that this electrostatic effect also influences the quaternary structure of PrP 27-30. Determining the secondary and tertiary structural differences in PrP 27-30 that give rise to rods or crystals will require additional purification because even the best 2D crystal preparations still contain substantial numbers of prion rods.

The reciprocal relationship between prion rods and 2D crystals shown in Fig. 4*A* requires qualification: purified samples were used for counting the number of 2D crystals and crude fractions were used for determining the number of rods (see also *SI Methods*). To obtain reproducible results, the samples for rod counts were taken immediately after the fibrillization reaction and before centrifugation. This step prevented the prion rods from aggregating and allowed us to distinguish individual fibrils and small clusters of fibrils at relatively low magnifications (of 1,700 to 5,000×). In contrast, the 2D crystals could only be identified at higher magnifications (>25,000×), which made it necessary to use concentrated samples. Currently, we have no reliable means to calculate the precise number of PrP 27-30 molecules per length of prion rod because key aggregation parameters are unknown. Although we know the lattice parameters of the 2D crystals, the thickness of the crystals is unknown. Once the packing arrangement of the PrP 27-30 molecules in the prion rods is understood and the thickness of the 2D crystals can be determined, it will be possible to calculate more accurate comparisons.

The discovery reported here that PTA favors rod assembly and HTA favors crystal formation should provide tools that can be used to answer several fundamental questions about the prion polymerization pathways. Can prion rods be converted into crystals by exposure to HTA? Can crystals be transformed into rods by using PTA? Can conditions be identified in which all PrP 27-30 polymers are crystals? Given the formation of lacunary structures, what are the species of PTA and HTA that actually bind to PrP 27-30? We do not know whether it will be possible to convert crystals into soluble, oligomeric complexes composed of native PrP^{Sc}. Attempts to solubilize native PrP^{Sc} from rods have been disappointing (10, 35, 36) although a small fraction of low-molecular-weight prions can be recovered after size fractionation (37).

Earlier experimental and computational analyses of the 2D crystals argue for a trimer of parallel left-handed, β-helices as the fundamental unit of PrP^{Sc} structure (12, 38). This model is consistent with ionization radiation experiments, which identified the target size of the proteinaceous part of the smallest infectious unit as being 55 ± 9 kDa (39, 40). For comparison, the molecular mass of trimers of the polypeptide chains of PrP^{Sc} and PrP 27-30 are 69 and 48 kDa, respectively.

The use of POMs to manipulate the polymeric forms of PrP 27-30 is particularly intriguing because it may be possible to create conditions where PrP^{Sc} polymerizes into 3D crystals that are suitable for high-resolution X-ray structure determination. The mechanism by which HTA stimulates 2D crystal formation is unknown. One factor may be the apparent ability of HTA precipitation to reduce the impurities in purified fractions compared with PTA (Fig. 1*E*). It is possible that, as the rods are elongated, they trap more impurities than crystals do as they form. The ability to fine-tune the molecular properties of the POM particles, as demonstrated by changes in the valency of the central heteroatom that resulted in increased charge densities, improves their versatility as tools to study the structure of oligomeric and polymeric protein assemblies. The use of HTA or

a POM with an even higher surface-charge density might be ideal for encouraging large 3D crystal formation.

Methods

Immunoassays, preparation of 2D crystals and POM stock solutions, image processing, fibril and 2D crystal content determinations, and statistical analysis are described in the *SI Methods*.

POM Precipitation of RML and Sc237 Prions. PrP 27-30 was prepared from the brains of scrapie-sick, wild-type FVB mice infected with RML prions or Syrian hamsters infected with Sc237 prions. The PTA precipitation protocols were based on published procedures (17). Ten percent brain homogenates (BH) were prepared in Ca^{2+}/Mg^{2+}-free PBS. Homogenates were clarified by centrifugation at 500 $\times$ *g* for 5 min in a tabletop centrifuge. The resulting supernatant was diluted to a final 5% (wt/vol) by using PBS containing 4% (wt/vol) Sarkosyl. The diluted samples were digested with 25 μg/mL proteinase K (PK) for 60 min at 37 °C with constant agitation. After incubation, protease inhibitors (0.5 mM PMSF; aprotinin and leupeptin, 2 μg/mL each) were added and the samples were mixed with the POM stock solutions. After either 1 or 16 h of incubation at 37 °C on a rocking platform, the samples were centrifuged at 14,000 $\times$ *g* for 30 min at room temperature (RT). The resulting pellets were resuspended in PBS containing 2% Sarkosyl and the precipitation was repeated with the same concentration of POM. The final pellet was resuspended in PBS with 0.2% Sarkosyl containing protease inhibitors (see above).

For the quantification of the 2D crystal contents, 20% BH was used instead of the usual 10% and the clarified supernatant was adjusted to 10% BH equivalent before the addition of the POM stock solutions. This variation in the protocol ensured a more reliable production of 2D crystals.

Electron Microscopy. Negative staining was performed on Formvar/carbon-coated, 200-mesh copper grids (Ted Pella, Inc.) that were glow-discharged before staining. Five-microliter samples were adsorbed for 30 s, briefly washed with 0.1 M and 0.01 M ammonium acetate buffer, pH 7.4, and stained with 2 drops (50 μL each) of freshly filtered 2% (wt/vol) uranyl acetate (41). Positively stained samples relied on the contrast provided by the POMs used to precipitate PrP 27-30. Samples were loaded onto the grids, adsorbed, and washed with ammonium acetate buffers as described above, but without any additional staining steps. After drying, the samples were viewed with a FEI Tecnai F20 electron microscope (FEI Company) at an acceleration voltage of 80 kV. Electron micrographs were recorded on a Gatan UltraScan 4000 CCD camera.

ImmunoGold Labeling of the 2D Crystals. ImmunoGold labeling was performed essentially as described in refs. 12 and 42. To reduce the background intensity, denatured forms of PrP were removed by briefly incubating the grid with 50 μg/mL PK for 15 min at RT. To enhance the labeling intensity, antibodies were incubated for 2 h.

ACKNOWLEDGMENTS. We thank the staff of the Hunters Point Animal Facility for their expert animal studies; Diane Latawiec, Camille Deering, and Ana Serban [University of California, San Francisco (UCSF)] for their assistance in producing the different PrP 27-30 preparations and for providing the monoclonal antibodies; Robert Chalkley (UCSF mass spectrometry facility) for mass spectrometric analyses; and Hang Nguyen for her skillful editorial assistance. This work was supported by National Institutes of Health Grants AG02132, AG10770, and AG021601, by the Sherman Fairchild Foundation, and by the G. Harold and Leila Y. Mathers Charitable Foundation.

1. Collinge J, Clarke AR (2007) A general model of prion strains and their pathogenicity. *Science* 318:930–936.
2. Prusiner SB (2007) Prions. *Fields Virology*, eds Knipe DM, *et al.* (Lippincott Williams & Wilkins, Philadelphia), 5th Ed, pp 3059–3092.
3. Caughey BW, *et al.* (1991) Secondary structure analysis of the scrapie-associated protein PrP 27–30 in water by infrared spectroscopy. *Biochemistry* 30:7672–7680.
4. Pan K-M, *et al.* (1993) Conversion of α-helices into β-sheets features in the formation of the scrapie prion proteins. *Proc Natl Acad Sci USA* 90:10962–10966.
5. Prusiner SB, *et al.* (1983) Scrapie prions aggregate to form amyloid-like birefringent rods. *Cell* 35:349–358.
6. Stahl N, Borchelt DR, Hsiao K, Prusiner SB (1987) Scrapie prion protein contains a phosphatidylinositol glycolipid. *Cell* 51:229–240.
7. Pan K-M, Stahl N, Prusiner SB (1992) Purification and properties of the cellular prion protein from Syrian hamster brain. *Protein Sci* 1:1343–1352.
8. Govaerts C, Wille H, Prusiner SB, Cohen FE (2004) Structural studies of prion proteins. *Prion Biology and Diseases*, ed Prusiner SB (Cold Spring Harbor Lab Press, Cold Spring Harbor, NY), 2nd Ed, pp 243–282.
9. Harris DA, True HL (2006) New insights into prion structure and toxicity. *Neuron* 50:353–357.
10. Prusiner SB, *et al.* (1982) Further purification and characterization of scrapie prions. *Biochemistry* 21:6942–6950.
11. Wille H, *et al.* (2002) Structural studies of the scrapie prion protein by electron crystallography. *Proc Natl Acad Sci USA* 99:3563–3568.
12. Wille H, *et al.* (2007) Electron crystallography of the scrapie prion protein complexed with heavy metals. *Arch Biochem Biophys* 467:239–248.
13. Peretz D, *et al.* (1997) A conformational transition at the N-terminus of the prion protein features in formation of the scrapie isoform. *J Mol Biol* 273:614–622.
14. Eghiaian F, *et al.* (2004) Insight into the $PrP^{C} \rightarrow PrP^{Sc}$ conversion from the structures of antibody-bound ovine prion scrapie-susceptibility variants. *Proc Natl Acad Sci USA* 101:10254–10259.
15. Oesch B, *et al.* (1985) A cellular gene encodes scrapie PrP 27-30 protein. *Cell* 40:735–746.
16. Barry RA, Prusiner SB (1986) Monoclonal antibodies to the cellular and scrapie prion proteins. *J Infect Dis* 154:518–521.
17. Safar J, *et al.* (1998) Eight prion strains have PrP^{Sc} molecules with different conformations. *Nat Med* 4:1157–1165.
18. Lee IS, Long JR, Prusiner SB, Safar JG (2005) Selective precipitation of prions by polyoxometalate complexes. *J Am Chem Soc* 127:13802–13803.
19. Keggin (1933) Structure of the molecule of 12-phosphotungstic acid. *Nature* 131:908–909.
20. Kühlbrandt W (2003) Two-dimensional crystallization of membrane proteins: A practical guide. *Membrane Protein Purification and Crystallization: A Practical Guide*, eds Hunte C, von Jagow G, Schägger H (Academic, New York), 2nd Ed, pp 253–284.
21. Schmidt-Krey I (2007) Electron crystallography of membrane proteins: Two-dimensional crystallization and screening by electron microscopy. *Methods* 41:417–426.
22. Pope MT (2004) Polyoxo anions: Synthesis and structure. *Comprehensive Coordination Chemistry II*, ed Wedd AG (Elsevier, San Diego), 2nd Ed, Vol 4, pp 635–678.
23. Long DL, Burkholder E, Cronin L (2007) Polyoxometalate clusters, nanostructures and materials: From self assembly to designer materials and devices. *Chem Soc Rev* 36:105–121.
24. Hill CL (2004) Polyoxometalates: Reactivity. *Comprehensive Coordination Chemistry II*, ed Wedd AG (Elsevier, San Diego), 2nd Ed, Vol 4, pp 679–759.
25. Safar JG, *et al.* (2005) Diagnosis of human prion disease. *Proc Natl Acad Sci USA* 102:3501–3506.
26. Waugh DF (1954) Protein-protein interactions. *Adv Protein Chem* 9:325–437.
27. Brange J, Andersen L, Laursen ED, Meyn G, Rasmussen E (1997) Toward understanding insulin fibrillation. *J Pharm Sci* 86:517–525.
28. Lansbury PT Jr, Caughey B (1996) The double life of the prion protein. *Curr Biol* 6:914–916.
29. Baskakov IV, Legname G, Baldwin MA, Prusiner SB, Cohen FE (2002) Pathway complexity of prion protein assembly into amyloid. *J Biol Chem* 277:21140–21148.
30. Colby DW, *et al.* (2007) Prion detection by an amyloid seeding assay. *Proc Natl Acad Sci USA* 104:20914–20919.
31. Dobson CM (2003) Protein folding and misfolding. *Nature* 426:884–890.
32. Wetzel R (2006) Kinetics and thermodynamics of amyloid fibril assembly. *Acc Chem Res* 39:671–679.
33. Zhang G, *et al.* (2007) Polyoxometalate binding to human serum albumin: A thermodynamic and spectroscopic approach. *J Phys Chem B* 111:11253–11259.
34. Lundqvist M, *et al.* (2008) Nanoparticle size and surface properties determine the protein corona with possible implications for biological impacts. *Proc Natl Acad Sci USA* 105:14265–14270.
35. McKinley MP, Braunfeld MB, Bellinger CG, Prusiner SB (1986) Molecular characteristics of prion rods purified from scrapie-infected hamster brains. *J Infect Dis* 154:110–120.
36. Wille H, Prusiner SB (1999) Ultrastructural studies on scrapie prion protein crystals obtained from reverse micellar solutions. *Biophys J* 76(2):1048–1062.
37. Silveira JR, *et al.* (2005) The most infectious prion protein particles. *Nature* 437:257–261.
38. Govaerts C, Wille H, Prusiner SB, Cohen FE (2004) Evidence for assembly of prions with left-handed β-helices into trimers. *Proc Natl Acad Sci USA* 101:8342–8347.
39. Bellinger-Kawahara CG, Kempner E, Groth DF, Gabizon R, Prusiner SB (1988) Scrapie prion liposomes and rods exhibit target sizes of 55,000 Da. *Virology* 164:537–541.
40. Kempner ES, Miller JH, McCreery MJ (1986) Radiation target analysis of glycoproteins. *Anal Biochem* 156:140–146.
41. Wille H, Zhang G-F, Baldwin MA, Cohen FE, Prusiner SB (1996) Separation of scrapie prion infectivity from PrP amyloid polymers. *J Mol Biol* 259:608–621.
42. Leffers KW, *et al.* (2005) Assembly of natural and recombinant prion protein into fibrils. *Biol Chem* 386:569–580.